Subpicotesla atomic magnetometry with a microfabricated vapour cell

VISHAL SHAH[1,2], SVENJA KNAPPE[1], PETER D. D. SCHWINDT[3] AND JOHN KITCHING[1]*

[1]National Institute of Standards and Technology, 325 Broadway, Boulder, Colorado 80305, USA
[2]Department of Physics, University of Colorado, Boulder, Colorado 80309, USA
[3]Sandia National Laboratories, MS 1082, PO Box 5800, Albuquerque, New Mexico 87185, USA
*e-mail: kitching@boulder.nist.gov

Published online: 1 November 2007; doi:10.1038/nphoton.2007.201

Highly sensitive magnetometers capable of measuring magnetic fields below 1 pT have an impact on areas as diverse as geophysical surveying[1], the detection of unexploded ordinance[2], space science[3], nuclear magnetic resonance[4,5], health care[6] and perimeter and remote monitoring. Recently, it has been shown that laboratory optical magnetometers[7,8], based on the precession of the spins of alkali atoms in the vapour phase, could achieve sensitivities in the femtotesla range, comparable to[9–12], or even exceeding[13], those of superconducting quantum interference devices[6]. We demonstrate here an atomic magnetometer based on a millimetre-scale microfabricated alkali vapour cell with sensitivity below 70 fT Hz$^{-1/2}$. Additionally, we use a simplified optical configuration that requires only a single low-power laser. This result suggests that millimetre-scale, low-power femtotesla magnetometers are feasible, and we support this proposition with a simple sensitivity scaling analysis. Such an instrument would greatly expand the range of applications in which atomic magnetometers could be used.

For decades, superconducting quantum interference device (SQUID) magnetometers have been unrivalled in their ability to measure low-frequency magnetic fields with extremely high precision. Optical magnetometers now share this spotlight, with demonstrated sensitivities below 1 fT Hz$^{-1/2}$ in a laboratory setting. This level of sensitivity has helped open the door to the application of atomic magnetometers to imaging of heart[14] and brain tissue[15] and the detection of nuclear magnetic resonance (NMR) and nuclear quadrupole resonance (NQR)[4,5,16]. The key physics that underlies several recent advances in optical magnetometry is the suppression of spin relaxation originating from spin-exchange collisions between the alkali atoms[17] and the generation of a large ground-state atomic polarization at low magnetic-field strengths. Operation of the magnetometer in this spin-exchange-relaxation-free (SERF) regime allows for spin-relaxation times over 10 ms, even at alkali atom densities above 10^{14} cm^{-3}, and suggests even better sensitivities may be achieved in future instruments.

Despite the exceptional progress in improving the sensitivity of these instruments in a laboratory setting, they remain large, complex and difficult to assemble and operate for extended periods. Recently, a highly miniaturized atomic magnetic sensor was demonstrated that was fabricated using the techniques of microelectromechanical systems[18] (MEMS). This early device was 12 mm^3 in volume and had a sensitivity of 50 pT Hz$^{-1/2}$. A better optimized chip-scale magnetometer of similar size but with a sensitivity of 5 pT Hz$^{-1/2}$ was demonstrated more recently[19], as was an evanescent-wave device with a sensitivity in the 10 pT Hz$^{-1/2}$ range[20].

The vapour cell used in this experiment, shown in Fig. 1a, had interior dimensions of 3 mm × 2 mm × 1 mm and was fabricated with a MEMS process as described previously[21,22]. The zero-field magnetic resonance was measured by means of optical absorption of a single circularly polarized light field[23] propagating in a direction perpendicular to the static magnetic field, B_0 (Fig. 1b). The magnetic resonance, shown in Fig. 1c, has a full-width at half-maximum of 83 nT (corresponding to 580 Hz) and a transmission contrast of 40%. The linewidth obtained by extrapolating to zero light intensity was around 15 nT (105 Hz). This linewidth is lower by a factor of 50 than the estimated spin-exchange-limited linewidth at this alkali atom density and corresponds closely to the linewidth limited by alkali–buffer-gas spin destruction[10,24]. This clearly indicates that the magnetometer is operating in the SERF regime.

From the resonance characteristics and noise level, a magnetic-field equivalent noise spectrum was determined and is shown by the red trace in Fig. 1d. Throughout much of the spectrum between 10 Hz and 200 Hz, the noise is found to be below 70 fT Hz$^{-1/2}$. This SERF measurement represents an improvement by a factor of almost 100 over previous results in microfabricated vapour cells[19]. Excess amplitude noise from the laser is thought to be the main factor limiting sensitivity in the single-beam configuration. For comparison, the sensitivity obtained under similar conditions using an orthogonal pump–probe configuration[13] is shown by the grey trace in Fig. 1d. The reduced noise in the 100–200-Hz band occurs in part because the laser-amplitude noise is suppressed by the differential detection in the Faraday rotation measurement. The use of a single-light-field configuration leads to a considerable simplification in the optical arrangement when compared with the two-beam pump–probe configuration, but suffers from increased susceptibility to laser-amplitude noise. We note, however, that laser-amplitude noise cancellation can be achieved in the single-beam configuration when the system is operated in the gradiometer mode or when the optical power at the entrance to the cell is monitored.

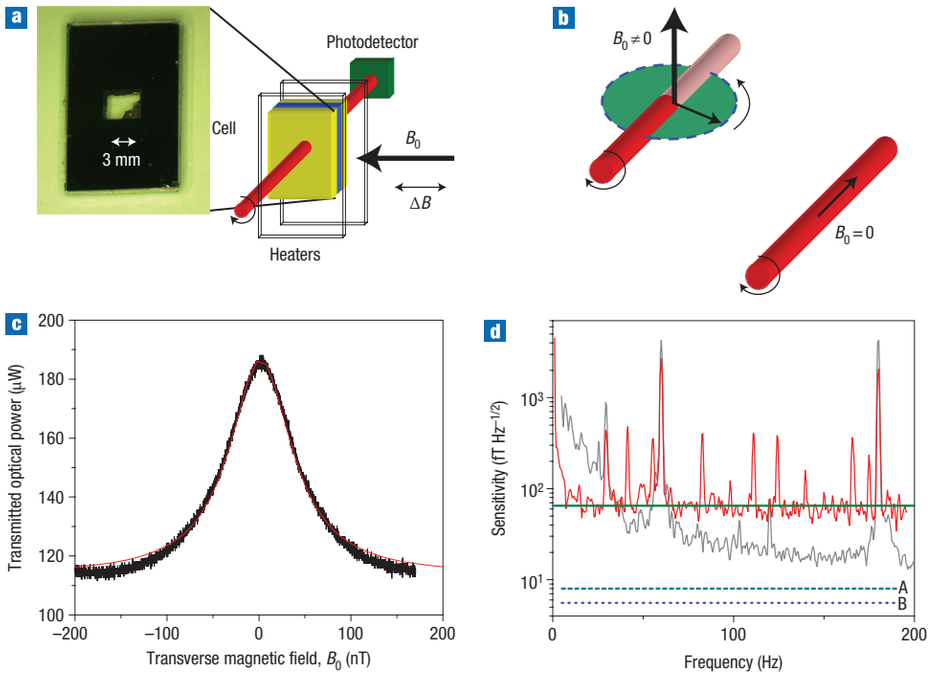

Figure 1 Atomic magnetometry with a micromachined alkali vapour cell. a, Schematic of the measurement apparatus. **b**, Orientation and dynamics of the atomic spins (blue arrows) as a function of B_0. **c**, A resonance is observed as the local field, B_0, is scanned about zero. The red line indicates a lorentzian fit with a full-width at half-maximum of 83 nT. **d**, Magnetic-field sensitivity for the single-beam geometry (red trace) and the two-beam geometry (grey trace) at $B_0 = 0$. The solid horizontal line indicates a sensitivity of 65 fT Hz$^{-1/2}$, and the dashed lines indicate the estimated sensitivity owing to photon shot noise (A, single-beam geometry; B, two-beam geometry).

The results presented above show that a SERF magnetometer with a sensitivity below 100 fT Hz$^{-1/2}$ is feasible in a MEMS alkali vapour cell using a simple, single-beam optical configuration. The optical design and the components used in this experiment are similar to those used in the miniature atomic magnetometers described in refs 18 and 19. This suggests that highly sensitive SERF magnetometers can be made equally small and low in power by using similar MEMS fabrication techniques. Magnetic noise originating from electric currents in the various active and passive components will undoubtedly be more important for highly compact devices. Our estimations, however, suggest that this noise is either negligible on a millimetre length scale or can be mitigated with minor modifications to the optical design or the electronic packaging.

To guide designs for future MEMS-based instruments, we consider now how the sensitivity of such a magnetometer, and the power required to run it, scale with the size of the cell. Some applications, such as magnetoencephalography, can tolerate high operating powers but require high sensitivity, but other applications, such as remote monitoring, require low operating power to enable a long instrument lifetime with battery operation. The fundamental limit on the sensitivity of an atomic magnetometer due to atom shot noise in the regime in which the resonance linewidth is limited by spin-exchange collisions can be stated as[10]

$$\delta B_{\min} \approx \frac{1}{\gamma}\sqrt{\frac{\bar{v}\sigma_{\mathrm{SR}}}{Vt}} \qquad (1)$$

where γ is the gyromagnetic constant of the atoms, $\bar{v}$ is the mean relative velocity, σ_{SR} is the spin relaxation cross-section, V is the cell volume and t is the integration time. The scaling of the atom-shot-noise-limited magnetometer sensitivity is plotted in Fig. 2a as a function of cell size under the condition that the electron-spin relaxation rate ($n\sigma_{\mathrm{SR}}\bar{v}$, where n is the alkali atom density) is equal to the combined relaxation rate due to wall and buffer-gas collisions and that the relaxation rates due to wall and buffer-gas collisions are themselves equal. Note that the cell temperature that satisfies this condition varies with the size of the cell. Under SERF conditions (low magnetic fields), the spin relaxation rate is determined by the alkali–alkali spin-destruction collision cross-section ($\sim 9 \times 10^{-18}$ cm^2 for ^{87}Rb), but under spin-exchange-limited conditions (high magnetic fields), this rate is determined by the alkali–alkali spin-exchange cross-section ($\sim 2 \times 10^{-14}$ cm^2 for ^{39}K, ^{87}Rb and ^{133}Cs), with both relaxation rates modified by the appropriate nuclear slow-down factor. In Fig. 2, we assume no nuclear slow-down of the relaxation rate for simplicity, but recognize that the magnetometer sensitivity may be somewhat better than that shown in Fig. 2a owing to this effect. Subpicotesla sensitivities can in principle be achieved for cell sizes as small as 10 μm for ^{39}K under SERF conditions, and subfemtotesla sensitivities can be achieved for millimetre-scale cells. In practice, other noise sources such as photon shot noise and laser-amplitude and frequency noise significantly degrade the magnetometer sensitivity. In the experiment described above, the signal-to-noise ratio is approximately 1×10^6 in a 1-Hz bandwidth.

We may evaluate the alkali density at which the relaxation rate due to alkali–alkali collisions (determined by the spin-exchange or

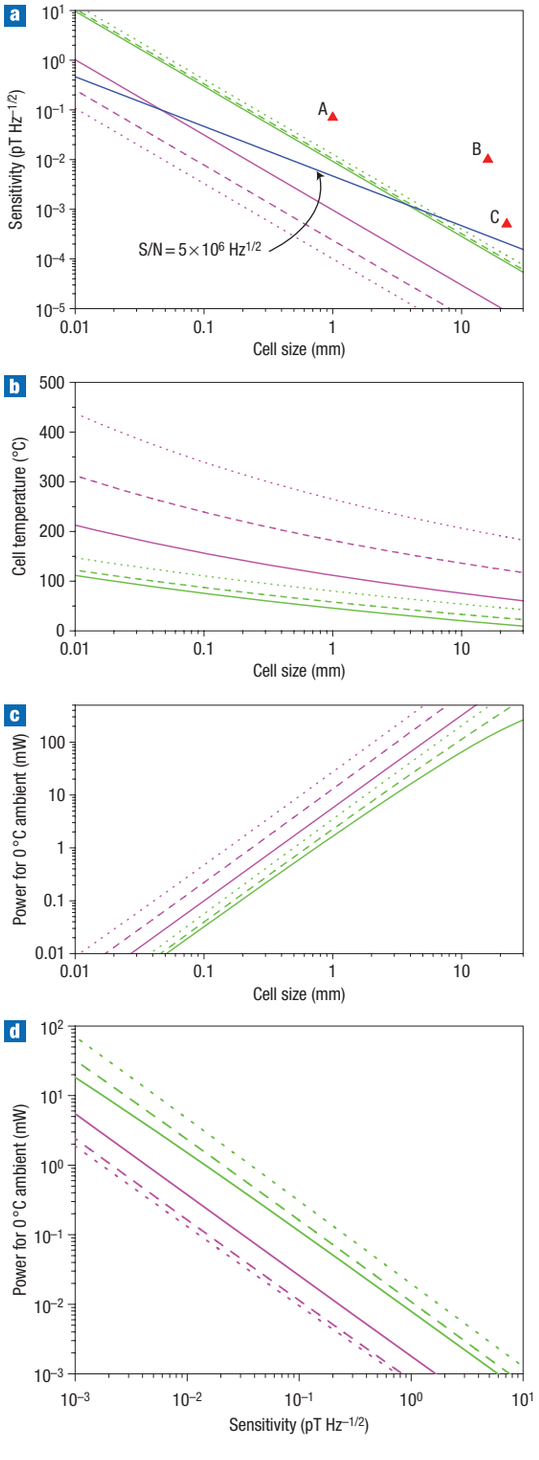

Figure 2 Magnetometer sensitivity scaling under near-optimal conditions for linewidth. Lines indicate ^{133}Cs (solid lines), ^{87}Rb (dashed lines) and ^{39}K (dotted lines) under spin-exchange-limited conditions (green) and SERF conditions (magenta). **a**, Sensitivity as a function of cell size; limit due to shot noise on 10 μW of power and unity signal contrast (blue line). Experimental data points (filled triangles) A, B and C correspond to this work, refs 10, 13, respectively. **b**, Corresponding cell temperature assuming an optimized buffer gas of Ne, and no nuclear slow-down. **c**, Corresponding cell heating power based on the design of ref. 27. **d**, Cell heating power required as a function of desired sensitivity.

spin-destruction cross-sections as appropriate) is equal to the combined relaxation rate due to atom diffusion and buffer-gas collisions. The corresponding cell temperature can be determined from standard vapour pressure curves. This cell temperature is plotted as a function of cell size in Fig. 2b. In well-engineered MEMS-based atomic instruments, the power required to run the device, P_{diss}, is expected to be dominated by that required to heat the cell to its operating temperature[25,26], which is in turn dominated by radiative heat loss[27]. To estimate this power, we calculate the radiative loss from a cubic black body with volume equal to that of the cell and at a temperature determined by Fig. 2b. In Fig. 2c P_{diss} is plotted as a function of cell size. The results of Fig. 2a are combined with those in Fig. 2c to generate a plot of the expected power requirement as a function of desired sensitivity in Fig. 2d. Under SERF conditions and the assumptions stated above, a sensitivity near 10 fT Hz$^{-1/2}$ can in principle be achieved with under 10 mW of heating power for both ^{39}K and ^{87}Rb magnetometers. With low-emissivity coatings around the physics package, operation at even lower power levels could be obtained.

The demonstration of subpicotesla sensitivity in a MEMS-fabricated alkali vapour cell is particularly relevant with regard to applications of magnetometers. Our results suggest that portable, battery-operated and yet highly sensitive magnetic-field sensors are technologically viable. Such instruments may enable lower-cost non-invasive biomagnetic diagnostic measurements[6] such as fetal magnetocardiography[28] and array-based magnetoencephalography used to localize certain kinds of brain activity[29]. Of particular value here is the broad linewidth of the magnetic resonances in submillimetre vapour cells, which allows for detection bandwidths in the kilohertz range. Portable explosive detection systems are also possible based on NQR detection[16]. Battery-operated sensors could be deployed in remote locations to monitor the movement of magnetic objects such as vehicles or to measure geophysical anomalies. For this application, high dynamic range is important. Magnetometers based on small cells tend to be operated at higher cell temperatures and hence higher alkali atom densities than their larger counterparts (see Fig. 2b), which allows SERF operation over a wider range of magnetic fields. Finally, compact, high-performance gyroscopes[30] using techniques and components similar to those described here may also be feasible.

METHODS

CELL CONFIGURATION

The microfabricated vapour cell contains isotopically enriched ^{87}Rb at its vapour pressure and a N_2 buffer gas at a density of 3 amagat (1 amagat is the density in cm^{-3} of atoms of a perfect gas at standard temperature and pressure), and was heated to 152 °C with a pair of transparent resistive thin-film heaters placed over the cell windows. At this temperature, the alkali atom density estimated from vapour pressure curves was 1.5×10^{14} cm^{-3}, and the corresponding spin-exchange broadened linewidth was 8 kHz. The current passing through the heaters generated both a magnetic field and a field gradient at the location of the cell. To avoid complications due to this field, the current through the heaters was chopped on and off with a period of 8 s and 50% duty cycle, and all measurements were carried out when the heater currents were off.

RESONANCE AND NOISE MEASUREMENT

For the single-beam measurement, a circularly polarized laser beam of area 2.5 mm^2 and power 0.35 mW was tuned to the peak of the single pressure-broadened D1 absorption resonance in ^{87}Rb. The transmitted optical power is shown in Fig. 1c as a function of the transverse magnetic field. To avoid the effects of low-frequency electronic noise, a magnetic field varying sinusoidally at a frequency of 590 Hz was applied along the direction of the static magnetic field with a pair of external coils. The photodiode signal was demodulated with a lock-in amplifier, resulting in a dispersive error signal as a function of static field. The static field was tuned to the centre of this resonance (nominally zero field),

and the voltage noise spectrum measured under these conditions was converted into a magnetic-field equivalent noise spectrum, which is shown by the red trace in Fig. 1d.

In the two-beam measurement, the circularly polarized pump beam (0.3 mW) was tuned close to the optical resonance, and the linearly polarized probe field (0.12 mW) propagating in an orthogonal direction was detuned by ~3 GHz. The zero-field magnetic resonance was measured by optical Faraday rotation, and the corresponding sensitivity spectrum is shown by the grey trace in Fig. 1d.

POWER SCALING

If a MEMS-based physics package is placed inside an evacuated enclosure, thermal losses are determined entirely by conduction along the support structure and radiation. In some recently developed microfabricated atomic instruments (see for example, ref. 27), the support structure for the physics package had a low enough thermal conductance that radiation dominated the heat loss over a wide range of temperatures. The question arises as to how the ratio of radiative heat loss to conductive heat loss scales with the size of the physics package. The scaling of the heat lost from conduction through the supports is determined by the condition of a constant mechanical response ($\Delta L/L$) of the cell supports to an externally applied acceleration. Under this condition, the cross-sectional area of the cell supports, A, scales with the mass, and therefore the volume (L^3) of the cell, and the thermal conductance scales as $A/L \approx L^2$. The radiative heat loss is determined by the radiating surface area and therefore also scales as L^2. We therefore conclude that the ratio of radiative heat loss to conductive heat loss is largely independent of the size of the instrument and that the heat loss in a scaled version of the design of ref. 27 will continue to be dominated by radiation.

Based on this analysis, we estimate the power required to operate a compact magnetometer by calculating the power radiated by a cubic black body of volume $V = L^3$ according to

$$P_{\mathrm{diss}} = \varepsilon\sigma(6L^2)[T_{\mathrm{cell}}^4 - 273\,\mathrm{K}^4] \qquad (2)$$

where T_{cell} is the cell temperature in Kelvin, which is a function of the cell size L according to Fig. 2b, ε is the emissivity, assumed to be unity, and σ is the Stefan–Boltzmann constant.

Received 16 April 2007; accepted 27 August 2007; published 1 November 2007.

References

1. Cande, S. C., Raymond, C. A., Stock, J. & Haxby, W. F. Geophysics of the Pitman fracture zone and Pacific–Antarctic plate motions during the Cenozoic. *Science* **270,** 947–953 (1995).
2. Delaney, W. P. & Etter, D. Report of the Defense Science Board Task Force on Unexploded Ordinance, <http://www.acq.osd.mil/dsb/reports/uxo.pdf> (2003).
3. Acuna, M. H. Space-based magnetometers. *Rev. Sci. Instrum.* **73,** 3717–3736 (2002).
4. Savukov, I. M. & Romalis, M. V. NMR detection with an atomic magnetometer. *Phys. Rev. Lett.* **94,** 123001 (2005).
5. Xu, S. J. *et al.* Magnetic resonance imaging with an optical atomic magnetometer. *Proc. Natl Acad. Sci. USA* **103,** 12668–12671 (2006).
6. Fagaly, R. L. Superconducting quantum interference device instruments and applications. *Rev. Sci. Instrum.* **77,** 101101 (2006).
7. Dehmelt, H. G. Modulation of a light beam by precessing absorbing atoms. *Phys. Rev.* **105,** 1924–1925 (1957).
8. Bell, W. E. & Bloom, A. Optical detection of magnetic resonance in alkali metal vapor. *Phys. Rev.* **107,** 1559–1565 (1957).
9. Alexandrov, E. B., Balabas, M. V., Pasgalev, A. S., Vershovskii, A. K. & Yakobson, N. N. Double-resonance atomic magnetometers: From gas discharge to laser pumping. *Laser. Phys.* **6,** 244–251 (1996).
10. Allred, J. C., Lyman, R. N., Kornack, T. W. & Romalis, M. V. High-sensitivity atomic magnetometer unaffected by spin-exchange relaxation. *Phys. Rev. Lett.* **89,** 130801 (2002).
11. Budker, D., Kimball, D. F., Rochester, S. M., Yashchuk, V. V. & Zolotorev, M. Sensitive magnetometry based on nonlinear magneto-optical rotation. *Phys. Rev. A* **6204,** 043403 (2000).
12. Groeger, S., Bison, G., Schenker, J. L., Wynands, R. & Weis, A. A high-sensitivity laser-pumped M-x magnetometer. *Eur. Phys. J. D* **38,** 239–247 (2006).
13. Kominis, I. K., Kornack, T. W., Allred, J. C. & Romalis, M. V. A subfemtotesla multichannel atomic magnetometer. *Nature* **422,** 596–599 (2003).
14. Bison, G., Wynands, R. & Weis, A. Dynamical mapping of the human cardiomagnetic field with a room-temperature, laser-optical sensor. *Opt. Express* **11,** 904–909 (2003).
15. Xia, H., Baranga, A. B.-A., Hoffman, D. & Romalis, M. V. Magnetoencephalography with an atomic magnetometer. *Appl. Phys. Lett.* **89,** 211104 (2006).
16. Lee, S.-K., Sauer, K. L., Seltzer, S. J., Alem, O. & Romalis, M. V. Subfemtotesla radio-frequency atomic magnetometer for detection of nuclear quadrupole resonance. *Appl. Phys. Lett.* **89,** 214106 (2006).
17. Happer, W. & Tang, H. Spin-exchange shift and narrowing of magnetic resonance lines in optically pumped alkali vapors. *Phys. Rev. Lett.* **31,** 273–276 (1973).
18. Schwindt, P. D. D. *et al.* Chip-scale atomic magnetometer. *Appl. Phys. Lett.* **85,** 6409–6411 (2004).
19. Schwindt, P. D. D. *et al.* A chip-scale atomic magnetometer with improved sensitivity using the Mx technique. *Appl. Phys. Lett.* **90,** 081102 (2007).
20. Zhao, K. F. & Wu, Z. Evanescent wave magnetometer. *Appl. Phys. Lett.* **89,** 261113 (2006).
21. Liew, L. A. *et al.* Microfabricated alkali atom vapor cells. *Appl. Phys. Lett.* **84,** 2694–2696 (2004).
22. Knappe, S. *et al.* Atomic vapor cells for chip-scale atomic clocks with improved long-term frequency stability. *Opt. Lett.* **30,** 2351–2353 (2005).
23. Dupont-Roc, J., Haroche, S. & Cohen-Tannoudji, C. Detection of very weak magnetic fields (10^{-9} gauss) by ^{87}Rb zero-field level crossing resonances. *Phys. Lett. A* **28,** 638 (1969).
24. Baranga, A. B. A. *et al.* Polarization of He-3 by spin exchange with optically pumped Rb and K vapors. *Phys. Rev. Lett.* **80,** 2801–2804 (1998).
25. Knappe, S. *et al.* A microfabricated atomic clock. *Appl. Phys. Lett.* **85,** 1460–1462 (2004).
26. Kitching, J. *et al.* in *Proc. IEEE International Frequency Control Symposium* Montreal, PQ, 781–784 (2004).
27. Mescher, M. J., Lutwak, R. & Varghese, M. An ultra-low-power physics package for a chip-scale atomic clock. *Proc. Transducers '05, IEEE International Conference on Solid-State Sensors and Actuators*, Seoul, Korea (2005).
28. Quinn, A. *et al.* Antenatal fetal magnetocardiography—a new method for fetal surveillance. *Br. J. Obstet. Gynaecol.* **101,** 866–870 (1994).
29. Sato, S. *Magnetoencephalography: Comparison with Electroencephalography and Clinical Applications* (Raven, New York, 1990).
30. Kornack, T. W., Ghosh, R. K. & Romalis, M. V. Nuclear spin based gyroscope based on an atomic comagnetometer. *Phys. Rev. Lett.* **95,** 230801 (2005).

Acknowledgements

The authors acknowledge valuable discussions with L. Hollberg, M. Romalis and D. Budker and thank S. Schima and L. Liew for help with the cell fabrication. This work was funded by the National Institute of Standards and Technology (NIST), the Defense Advanced Research Projects Agency (DARPA) and the Strategic Environmental Research and Development Program (SERDP). This work is a partial contribution of NIST, an agency of the US government, and is not subject to copyright.

Author contributions

V.S. and P.D.D.S. carried out the experiments and noise analysis, S.K. fabricated the alkali vapour cell, and J.K. carried out the scaling analysis.